

# Game of Learning Bloch Equation Simulations for MR Fingerprinting

Mingrui Yang<sup>1,\*</sup>, Yun Jiang<sup>2</sup>, Dan Ma<sup>2</sup>, Bhairav B. Mehta<sup>2</sup>, Mark A. Griswold<sup>2,3</sup>

1. Department of Biomedical Engineering, Cleveland Clinic, Cleveland, Ohio, USA
2. Department of Radiology, Case Western Reserve University, Cleveland, Ohio, USA
3. Department of Biomedical Engineering, Case Western Reserve University, Cleveland, Ohio, USA

\* Correspondence to:

Mingrui Yang  
Department of Biomedical Engineering  
Lerner Research Institute  
Cleveland Clinic  
9500 Euclid Ave  
Cleveland, OH 44106, USA  
Email: yangm@ccf.org

---

## Abstract

**Purpose:** This work proposes a novel approach to efficiently generate MR fingerprints for MR fingerprinting (MRF) problems based on the unsupervised deep learning model generative adversarial networks (GAN).

**Methods:** The GAN model is adopted and modified for better convergence and performance, resulting in an MRF specific model named GAN-MRF. The GAN-MRF model is trained, validated, and tested using different MRF fingerprints simulated from the Bloch equations with certain MRF sequence. The performance and robustness of the model are further tested by using in vivo data collected on a 3 Tesla scanner from a healthy volunteer together with MRF dictionaries with different sizes.  $T_1$ ,  $T_2$  maps are generated and compared quantitatively.

**Results:** The validation and testing curves for the GAN-MRF model show no evidence of high bias or high variance problems. The sample MRF fingerprints generated from the trained GAN-MRF model agree well with the benchmark fingerprints simulated from the Bloch equations. The in vivo  $T_1$ ,  $T_2$  maps generated from the GAN-MRF fingerprints are in good agreement with those generated from the Bloch simulated fingerprints, showing good performance and robustness of the proposed GAN-MRF model. Moreover, the MRF dictionary generation time is reduced from hours to sub-second for the testing dictionary.

**Conclusion:** The GAN-MRF model enables a fast and accurate generation of the MRF fingerprints. It significantly reduces the MRF dictionary generation process and opens the door for real-time applications and sequence optimization problems.

**Keywords:** MR fingerprinting, quantitative imaging, generative adversarial networks, dictionary generation, deep learning, machine learning

## Introduction

Magnetic resonance (MR) imaging has been a successful diagnostic imaging modality due to its ability to characterize a wide range of underlying tissue parameters. However, traditional MR images are generally qualitative, and can vary from scan to scan, leading to a variability in interpretation and limitation in objective evaluation. The aims of quantitative MR imaging is to eliminate this variability and limitation, and provide additional pathological information for diagnosis in a quantitative and deterministic manner. Conventional quantitative MR imaging methods for MR parameter (e.g.  $T_1$ ,  $T_2$ ,  $T_2^*$ ) mapping has had many successful applications in both research and clinical settings (16–18, 22, 24, 30, 33, 35–37). Most of these methods, however, can only evaluate one parameter of interest at a time, resulting in a prolonged scan time when multiple acquisitions have to be repeated to obtain different parameter maps for clinical applications.

Magnetic resonance fingerprinting (MRF) (25) is a newly developed quantitative magnetic resonance imaging method that may overcome some previous limitations of quantitative MR imaging (4–8, 10, 12, 29, 39–41). Unlike conventional quantitative MR imaging methods, MRF is able to efficiently obtain multiple tissue property maps simultaneously within one single scan. The collected raw data from a scanner is first reconstructed using e.g. nonuniform fast Fourier transform (11). The time dimension of each reconstructed voxel is then matched against a pre-calculated MRF dictionary using Bloch simulations, which is one of the key components of MRF. Depending on the tissue properties of interest, the dictionary can be calculated for different MRF sequences, such as the balanced steady-state free precession (bSSFP) (25) sequence, the fast imaging steady-state precession (FISP) (20) sequence, or the MRF-X (15) sequence. The size of the MRF dictionaries generated changes with the MRF sequence chosen and the step size used for certain tissue properties. It can be prohibitively large if complex sequences considering multiple tissue properties or fine step size for tissue properties are used. This can make the pattern matching stage of MRF significantly slowed down, or even worse, completely paralyzed due to lack of computer memory. Efforts have been taken to speed up the MRF pattern matching process (2, 27). These methods, however, still rely on a full sized MRF dictionary, and therefore, cannot resolve the memory consumption problem. Yang et al. (38) proposed to use the randomized singular value decomposition together with polynomial fitting methods to significantly reduce the memory overhead and speed up the pattern matching step of MRF problems. Nevertheless, none of these methods has considered the time needed to generate MRF dictionaries. In fact, the time required for generating these

dictionaries varies, but can be prohibitively long, especially when many factors are included into the calculation. For example, a slice profile corrected FISP dictionary requires the simulation of multiple spin evolutions which are then summed for each time frame to average out the effect of off resonance. Some dictionary calculations that involve exchange and other complicated physics can take days or even weeks to calculate (15, 26).

In this paper, we present a new approach to create MRF dictionaries with a significantly reduced time cost based on the recent development in the deep learning community. Specifically, we modify one of the most interesting unsupervised models, the generative adversarial networks (GAN) (14), into a semi-supervised model for our purpose, fed with tissue parameter combinations and sequence parameters. Given the trained GAN-MRF model, the problem of generating MRF dictionaries through the complicated Bloch equation simulations is transformed into easy matrix multiplications followed by some simple nonlinear activation functions. This transformation can significantly reduce the time needed to generate MRF dictionaries, which makes it possible to generate dictionaries with tissue properties of interest on-the-fly. We believe that this will open the door to the rapid calculation of dictionaries with more complex physics as well. In vivo 3T brain scan data are used to evaluate the quality of the MRF dictionaries generated.

## Theory

In this section, we present the details of the GAN model and its limitations. We then describe in detail our modified GAN-MRF model to possibly address these limitations. GAN is a newly

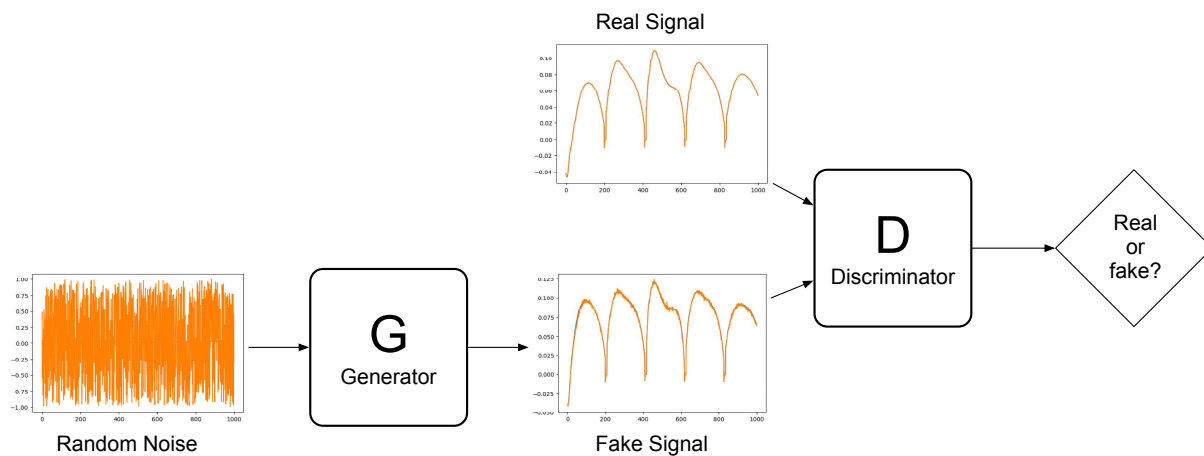


Figure 1: Generative Adversarial Network

developed unsupervised machine learning model, which has been vigorously studied in the past few years (3, 9, 13, 19, 23, 28, 31, 32, 34, 42). It basically contains a pair of networks competing with each other: a generative network (generator) and a discriminative network (discriminator). The generator is trained to synthesize data samples that mimic the real data from pure random noise to fool the discriminator; while the discriminator is trained to distinguish the real data samples from the synthesized samples generated by the generator, as illustrated in Fig. 1. They act as two players playing a minimax game and achieving the Nash equilibrium eventually.

Let us consider the generator  $G_{\theta_g}(z) : \mathbb{R}^m \rightarrow \mathbb{R}^n$  as a function mapping from a fixed prior noise distribution  $p(z)$  to the data space, and the discriminator  $D_{\theta_d}(x) : \mathbb{R}^n \rightarrow [0, 1]$  as a function mapping from the data space to a probability, where  $\theta_g$  and  $\theta_d$  are the parameters to estimate for the generator and discriminator networks respectively. Then the minimax objective function can be written as

$$\min_{\theta_g} \max_{\theta_d} [\mathbb{E}_{x \sim p_{data}} \log D_{\theta_d}(x) + \mathbb{E}_{z \sim p(z)} \log(1 - D_{\theta_d}(G_{\theta_g}(z)))] , \quad [1]$$

where  $x$  is drawn from the real data population  $p_{data}$ , and  $z$  is drawn from the prior noise distribution  $p(z)$ . Notice that this is a non-convex optimization problem. The convergence to the global optima cannot be guaranteed. A typical approach to solve this minimax optimization problem is to alternate between

$$\max_{\theta_d} [\mathbb{E}_{x \sim p_{data}} \log D_{\theta_d}(x) + \mathbb{E}_{z \sim p(z)} \log(1 - D_{\theta_d}(G_{\theta_g}(z)))] \quad [2]$$

and

$$\min_{\theta_g} \mathbb{E}_{z \sim p(z)} \log(1 - D_{\theta_d}(G_{\theta_g}(z))). \quad [3]$$

Note that solving [3] with the gradient descent algorithm is not efficient, since when the discriminator is not good, the gradient is small, which cannot provide sufficient information for the generator to evolve. Therefore, in practice, [3] is often transformed to an equivalent form

$$\max_{\theta_g} \mathbb{E}_{z \sim p(z)} \log D_{\theta_d}(G_{\theta_g}(z)) \quad [4]$$

for faster convergence.

The GAN model, although exciting, has several known issues. First of all, as mentioned above, the minimax problem [1] is a non-convex optimization problem, whose convergence to a global optima is not guaranteed. In other words, the problem may only converge to a local optima, or even worse, get stuck at a saddle point, which is neither a local maxima nor a local minima. Second, the model may collapse into a single mode so that the generator learns a pattern to generate a unique good looking fake data to fool the discriminator over and over again. Moreover, even if the GAN model does not collapse, the trained generator can only generate a limited number of distinct samples.

Our goal here is that, after the model is trained, we would like the generator to be able to synthesize a large variety of MR fingerprints corresponding to a wide range of tissue property and sequence parameter combinations. When used without modification, the limitations of the GAN model mentioned above dominate its performance, rendering it unable to fulfill our purpose. Therefore, we need to modify the GAN model for our purpose. It has been shown in the literature that the problems mentioned above can be partially solved by adding conditional information and regularization terms into the model (19, 28). We follow these ideas to modify the GAN model and write our GAN-MRF model as

$$\min_{\theta_g} \max_{\theta_d} \left[ \mathbb{E}_{x \sim p_{data}} \log D_{\theta_d}(x|y) + \mathbb{E}_{z \sim p(z)} \log(1 - D_{\theta_d}(G_{\theta_g}(z|y)|y)) + \lambda \mathbb{E}_{x \sim p_{data}, z \sim p(z)} \|x - G_{\theta_g}(z|y)\|_1 \right], \quad [5]$$

where  $x$  is drawn from the training fingerprints simulated from Bloch equations,  $y$  is the control variable concatenating the corresponding sequence parameters and tissue parameter combinations,  $z$  is drawn from the normal distribution  $\mathcal{N}(0, 1)$ , and  $\lambda$  is a hyperparameter controlling the regularization term. The conditional variable  $y$  can be a combination of, for instance, flip angle and repetition time, which are fed into the model in addition to the simulated fingerprints to better regulate the behavior of the model.  $\ell_1$  regularization is used since it is known to be more robust than e.g. the Euclidean distance regularization to noise and outliers, which is important for MR fingerprints generation. A small perturbation in an MR fingerprint can lead to completely different interpretation of the underlying tissue properties. The choice of the hyperparameter  $\lambda$  can be determined through a model validation process as explained in details in the Method section. The mini-max problem [5] is again a non-convex optimization problem, which can be solved by

alternating between

$$\max_{\theta_d} [\mathbb{E}_{x \sim p_{data}} \log D_{\theta_d}(x|y) + \mathbb{E}_{z \sim p(z)} \log(1 - D_{\theta_d}(G_{\theta_g}(z|y)|y))] \quad [6]$$

and

$$\max_{\theta_g} [\mathbb{E}_{z \sim p(z)} \log D_{\theta_d}(G_{\theta_g}(z|y)|y) - \lambda \mathbb{E}_{x \sim p_{data}, z \sim p(z)} \|x - G_{\theta_g}(z|y)\|_1]. \quad [7]$$

## Methods

### Data Generation

The data we used to train, validate, and test the GAN-MRF model was an MRF dictionary generated from Bloch equation simulations using a FISP sequence with slice profile correction (). The  $T_1$  values chosen for the simulations ranged from 10ms to 2950ms. The  $T_2$  values ( $\leq T_1$ ) range from 2ms to 500ms. They lead to a total tissue parameter combinations of 5970. The details of the ranges and step sizes of  $T_1$  and  $T_2$  values are listed in Table 1. The patterns of the flip angles and repetition time are shown in Fig. 2, with the flip angles ranging from 5 degrees to 70 degrees, and the repetition time ranging from 12.07ms to 14.73ms, resulting in a total of 1000 time frames. Note that the 1000 time frames are considered as 1000 features and the 5970  $T_1$ ,  $T_2$  combinations are considered as examples. The dataset was further divided into three parts including training data, validation data, and test data, so that each part contains 60%, 20%, and 20% of the total 5970 dictionary atoms respectively. The training, validation, and test sets were then normalized separately to avoid interference to the validation and test results from the training data.

### Model Specifics

The input layer of the discriminative network took MR fingerprints, ( either simulated from the Bloch equations with the FISP sequence, or synthesized by the generative network,) together with the corresponding  $T_1$  and  $T_2$  combinations. They were then passed through 3 hidden layers, each consisting of 128 neurons, followed by a rectified linear unit (ReLU). The output layer of the discriminative network outputted a probability of the input fingerprint being Bloch equations simulated by applying a sigmoid function as the activation function. The input layer of the generative network took pure random noise signals, together with the desired  $T_1$ ,  $T_2$  combinations and sequence

	Range	Step Size
$T_1$	[10, 85]	5
	[90, 990]	10
	[1000, 1480]	20
	[1500, 2000]	50
	[2050, 2950]	100
$T_2$	[2, 8]	2
	[10, 145]	5
	[150, 190]	10
	[200, 500]	50

Table 1: Ranges and step sizes of  $T_1$ ,  $T_2$  values. All in milliseconds (ms).

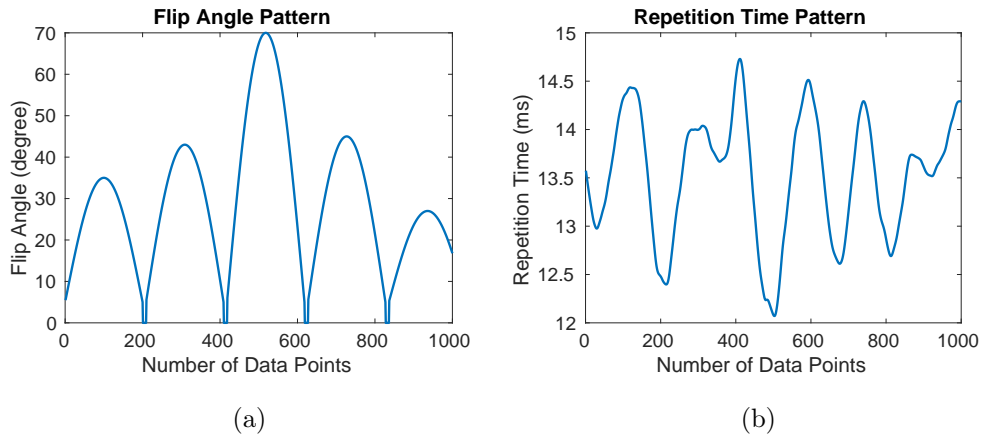


Figure 2: The patterns of the flip angle and repetition time used in the FISP sequence.

parameters such as flip angles and repetition time. Similar to the discriminative network, they were then passed through 3 hidden layers, each containing 128 neurons followed by a ReLU. The output layer of the generative network synthesized the corresponding MR fingerprints by utilizing a hyperbolic tangent function as the activation function. In summary, the discriminative network took training fingerprints and the associated sequence parameters and tissue property combinations to improve its performance in distinguishing real and synthesized fingerprints. The generative network only needed to know the input of sequence parameters and tissue parameter combinations of interest, and outputs the fingerprints that mimicking the real ones. A block diagram summarizing the GAN-MRF architecture is shown in Fig. 3.



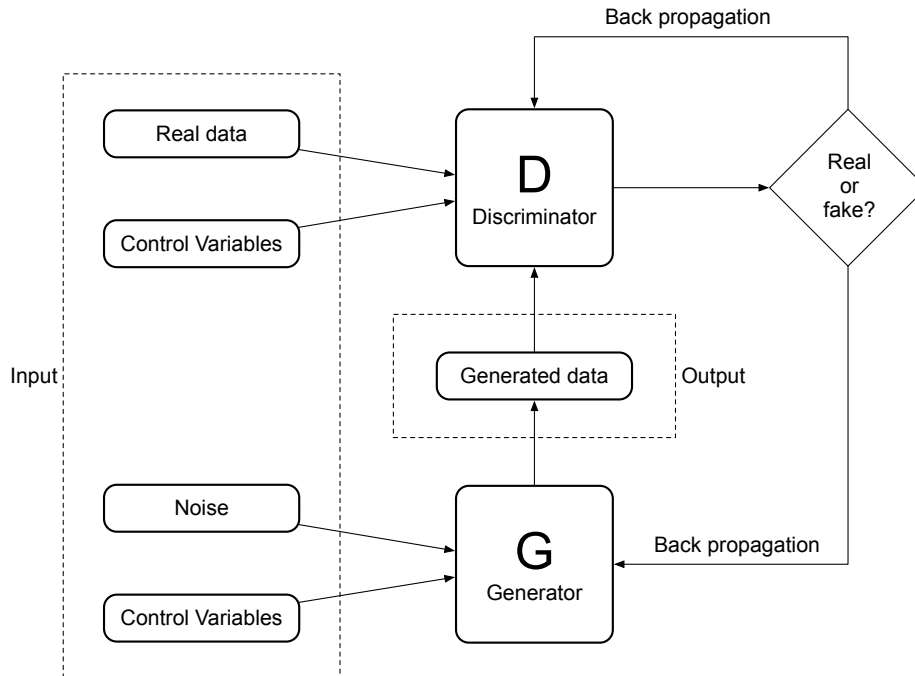


Figure 3: Flow chart for GAN-MRF

### Model Training, Validating, and Testing

The training, validation, and testing of the model were realized by using the Python deep learning framework Tensorflow (1) on a Ubuntu system with an Intel Xeon 2.6GHz CPU (Intel Corporation, Santa Clara, CA).

The discriminative network was trained by applying the stochastic gradient descent method to small batches of the training and synthesized data with the minibatch size equal to 30, using the Adam optimizer (21) with a learning rate of  $10^{-5}$ . The generative network was trained in the same fashion, but on small batches of random noise and training data. The loss functions for training the discriminative network and the generative network were modified versions of Eq. [6] and Eq. [7], where the maximization problems were converted into minimization problems by negating both [6] and [7].

The hyperparameter  $\lambda$  controlling model regularization in Eq. [7] was determined by running a model validation on the validation set. First, the root mean square errors between the training data and the synthesized data from the trained GAN-MRF model were calculated and plotted against difference choices of the values of the hyperparameter  $\lambda$ . Then, the root mean square errors between the validation data and the synthesized data generated from the trained model using the

validation control variables against different choices of  $\lambda$  were also computed and plotted. The  $\lambda$  value with the smallest validation root mean square error and fast convergence rate was chosen to be the hyperparameter value used in the loss function [7] for the generative network.

After the choice of the hyperparameter  $\lambda$  was determined, the trained GAN-MRF model was further tested on the test set independent of the training and validation sets for potential model underfitting or overfitting problems. Specifically, after each iteration, we calculated the root mean square errors between the synthesized fingerprints from the GAN-MRF model with the updated model parameters and the benchmark fingerprints from the training and test sets respectively. The root mean square errors were then plotted against the number of iterations to examine for indications of poor convergence, high bias or high variance problems.

### **In Vivo Test**

To test the performance of our model on *in vivo* dataset, a GAN-MRF dictionary was generated using the trained generative network with the same control variables used for the training, validation and test sets, resulting in a dictionary of size  $1000 \times 5970$ . The *in vivo* brain scan of a healthy volunteer was obtained on a Siemens Skyra 3T scanner (Siemens Healthcare, Erlangen, Germany) with a 20-channel head receiver coil array. The informed consent was obtained before the scan. All the experiments were approved by our institutional review board. The sequence used for the scan was the MRF-FISP sequence with the same sequence parameters and spiral sampling trajectory as previously reported (20) with an acceleration factor of 48 (one out of 48 spiral interleaves per repetition of MRF-FISP acquisition), a matrix size of  $256 \times 256$ , and a FOV of  $30 \times 30\text{cm}^2$ . The collected spiral data from each coil were reconstructed using the non-uniform fast Fourier transform with an independently measured spiral trajectory for gradient imperfection correction (11). Reconstructed images from all individual coils were then combined and compensated for coil sensitivity variation.  $T_1$ ,  $T_2$  maps were created by applying the standard MRF pattern matching algorithm between the reconstructed images and the GAN-MRF dictionary. The generated  $T_1$ ,  $T_2$  maps were then compared to the benchmark maps generated from the simulated MRF-FISP dictionary to compute the difference maps and the relative root mean square errors.

We further tested the scalability of our GAN-MRF model by first training the GAN-MRF model on a small training set simulated from Bloch equations. The trained model was then used to synthesize a much larger MRF dictionary with finer  $T_1$  and  $T_2$  step sizes. The synthesized dictionary was then used, together with the *in vivo* data, to perform the MRF pattern matching to obtain

the  $T_1$ ,  $T_2$  maps, which were compared against the maps obtained from the MRF-FISP dictionary by Bloch equation simulations with the same finer  $T_1$ ,  $T_2$  step sizes. More specifically, the coarse MRF-FISP dictionary (i.e. the training set) contained 1000 time frames and 297 tissue parameter combinations with the same  $T_1$ ,  $T_2$  ranges as in Table 1. We then generated a much finer GAN-MRF dictionary containing 106160 tissue property combinations using the trained model with an input of the refined  $T_1$ ,  $T_2$  combinations.  $T_1$  and  $T_2$  maps for the *in vivo* data were obtained from the synthesized fine GAN-MRF dictionary and compared against the ones generated from the MRF-FISP dictionary simulated directly from the Bloch equations with the refined  $T_1$ ,  $T_2$  combinations. The detailed step sizes of the coarse and fine  $T_1$  and  $T_2$  combinations are listed in Table 2.

	Coarse		Fine	
	Range	Step Size	Range	Step Size
$T_1$	[50, 100]	50	[2, 100]	2
	[200, 1000]	100	[105, 1000]	5
	[1200, 2000]	200	[1010, 2000]	10
	[2500, 3000]	500	[2025, 3000]	25
$T_2$	[10, 100]	10	[1, 200]	1
	[120, 200]	20	[202, 500]	2
	[300, 500]	100		

Table 2: Ranges and step sizes of  $T_1$ ,  $T_2$  values. All in milliseconds (ms).

## Results

The results for the GAN-MRF model training, validation, and testing are shown in Fig. 4. Specifically, Fig. 4a shows how the choice of the regularization hyperparameter  $\lambda$  in the minimax problem [5] can be determined by performing a model validation process. The training and validation root mean square errors with respect to different choice of the value of the hyperparameter  $\lambda$  that controls the regularization are plotted, where the blue solid curve represents the training error and the orange dashed curve represents the validation error. As shown in the plot, both the training and validation errors are large as the value of  $\lambda$  gets too small or too big. The training and validation errors are both small at  $\lambda = 1$  and  $\lambda = 100$ . We choose in our model  $\lambda$  to be 100 since it provides

better convergence. Fig. 4b shows the performance of the trained model on the training and test sets as the number of iterations increases in logarithmic scale. The blue solid curve represents the training error and the orange dashed curve represents the test error. One can see a clear decay in both the training and test errors, which indicates that there’s no evidence of high bias, or model under-fitting problem. In addition, the test error stays closely with the training error, indicating no evidence of high variance, or model over-fitting problems.

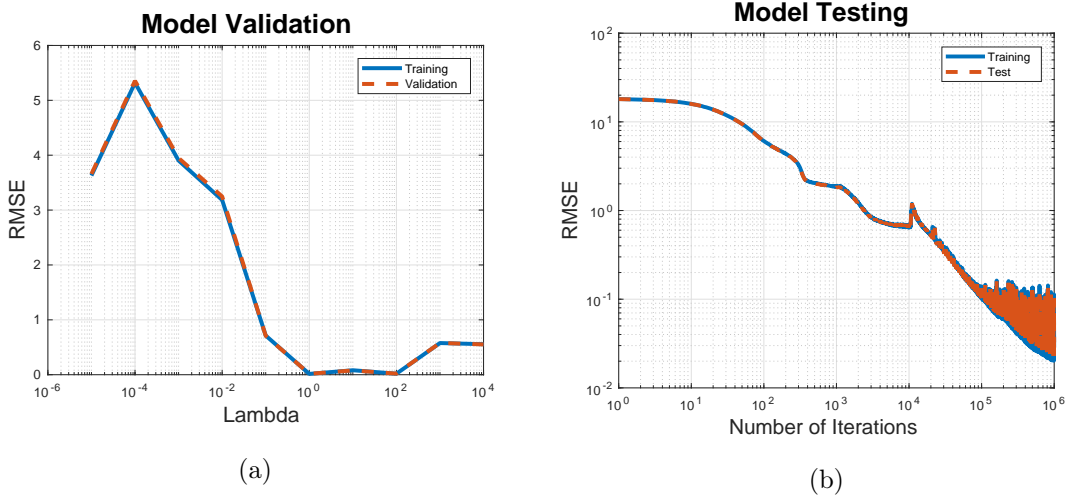


Figure 4: Model validation and testing

Fig. 5 shows several sample fingerprints generated by the proposed trained GAN-MRF model, where the orange curves represent the synthesized fingerprints using the GAN-MRF model, and the blue curves represent the benchmark MRF fingerprints simulated from Bloch equations. Fig. 5(a) plots a synthesized sample white matter GAN-MRF fingerprint with  $T_1 = 950\text{ms}$  and  $T_2 = 40\text{ms}$ , and compares it against the corresponding benchmark MRF fingerprint generated by Bloch simulations. Fig. 5(b) shows a sample gray matter fingerprint generated by the GAN-MRF model with  $T_1 = 1500\text{ms}$  and  $T_2 = 60\text{ms}$  and the corresponding gray matter benchmark MRF fingerprint. Fig. 5(c) shows a sample CSF fingerprint generated by the GAN-MRF model with  $T_1 = 2950\text{ms}$  and  $T_2 = 500\text{ms}$  and the corresponding CSF benchmark MRF fingerprint. Note that all these GAN-MRF fingerprints match to the MRF-FISP fingerprints well.

We further show the performance of the GAN-MRF model by comparing the in vivo  $T_1$  and  $T_2$  maps obtained using the GAN-MRF dictionary with the benchmark  $T_1$  and  $T_2$  maps obtained from the MRF-FISP dictionary generated by Bloch simulations. Shown in Fig. 6, column (a) are the benchmark  $T_1$  and  $T_2$  maps obtained by matching the collected in vivo data to the MRF-FISP

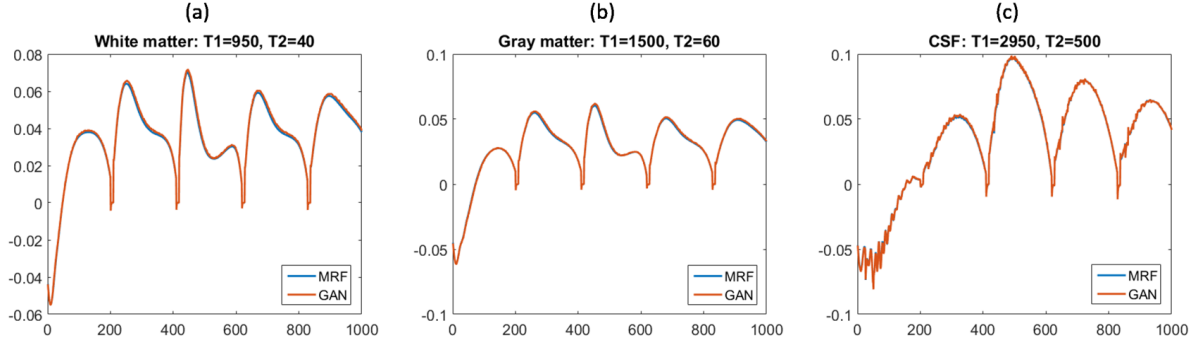


Figure 5: Sample fingerprints generated from GAN-MRF.

dictionary. Fig. 6 column (b) shows the  $T_1$  and  $T_2$  maps obtained by matching the collected in vivo data to the dictionary synthesized by the GAN-MRF model. They show no clear visual degradation from the benchmark  $T_1$  and  $T_2$  maps from the first column. The difference maps scaled 10 times are shown in Fig. 6 column (c). The relative root mean square error is only 0.55% for the  $T_1$  maps, and 2.66% for the  $T_2$  maps, which further confirm the finding.

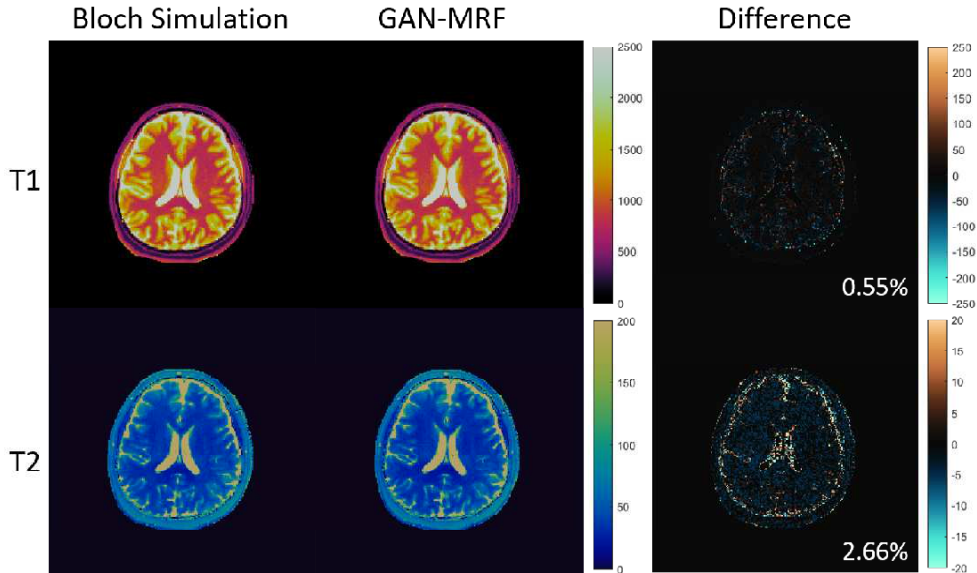


Figure 6: Comparison of maps generated from the MRF-FISP dictionary and the GAN-MRF dictionary.

Fig. 7 and Fig. 8 demonstrate the scalability of our GAN-MRF model. Specifically, Fig. 7 shows the in vivo  $T_1$ ,  $T_2$  maps, together with the corresponding difference maps, obtained from MRF dictionaries generated from 297  $T_1$ ,  $T_2$  combinations using the benchmark Bloch simulations and

the trained GAN-MRF model with the same input sequence and tissue parameters respectively. One observes that, as expected, the GAN-MRF model works well on this coarse dictionary. The relative root mean square error for  $T_1$  is 1.10% and for  $T_2$  is 3.51%. Next, Fig. 8 illustrates the robustness of the GAN-MRF model. Note that the model is trained on 297  $T_1$  and  $T_2$  combinations. The trained GAN-MRF model is then used to synthesize a dictionary corresponding to 106160 different  $T_1$ ,  $T_2$  combinations. The benchmark MRF-FISP dictionary is simulated from the Bloch equations using the same sequence parameters and the 106160  $T_1$ ,  $T_2$  combinations. Column (a) shows the in vivo  $T_1$ ,  $T_2$  maps generated from the benchmark MRF-FISP dictionary via pattern matching. Column (b) shows the  $T_1$  and  $T_2$  maps generated from the synthesized MRF dictionary using the coarsely trained MRF-GAN model. The difference maps are shown in column (c). We observe from these figures that by applying the GAN-MRF model trained on the coarse dictionary, we are still able to get decent  $T_1$ ,  $T_2$  maps compared to those obtained directly from the benchmark MRF-FISP dictionary with the same number of  $T_1$ ,  $T_2$  combinations. The relative root mean square error for  $T_1$  is now 1.69% and for  $T_2$  is 6.37%, which illustrate good interpolation ability of the trained GAN-MRF model.

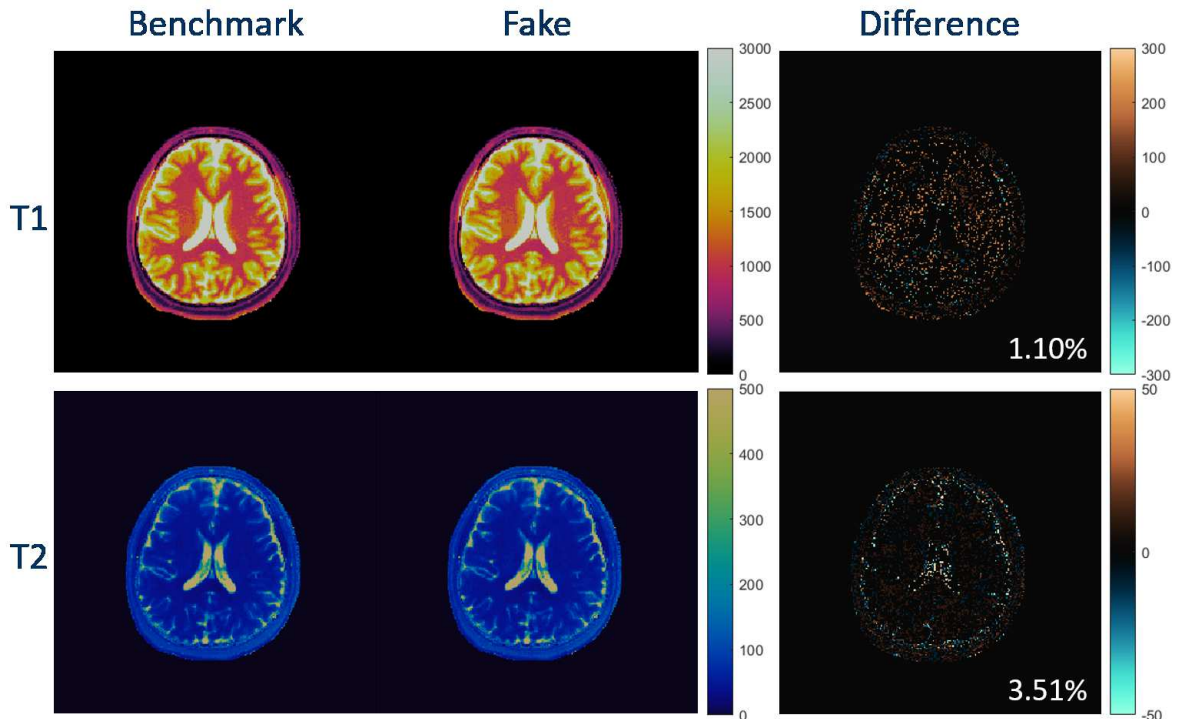


Figure 7: Comparison of maps generated from the coarse MRF-FISP dictionary and the GAN-MRF dictionary.

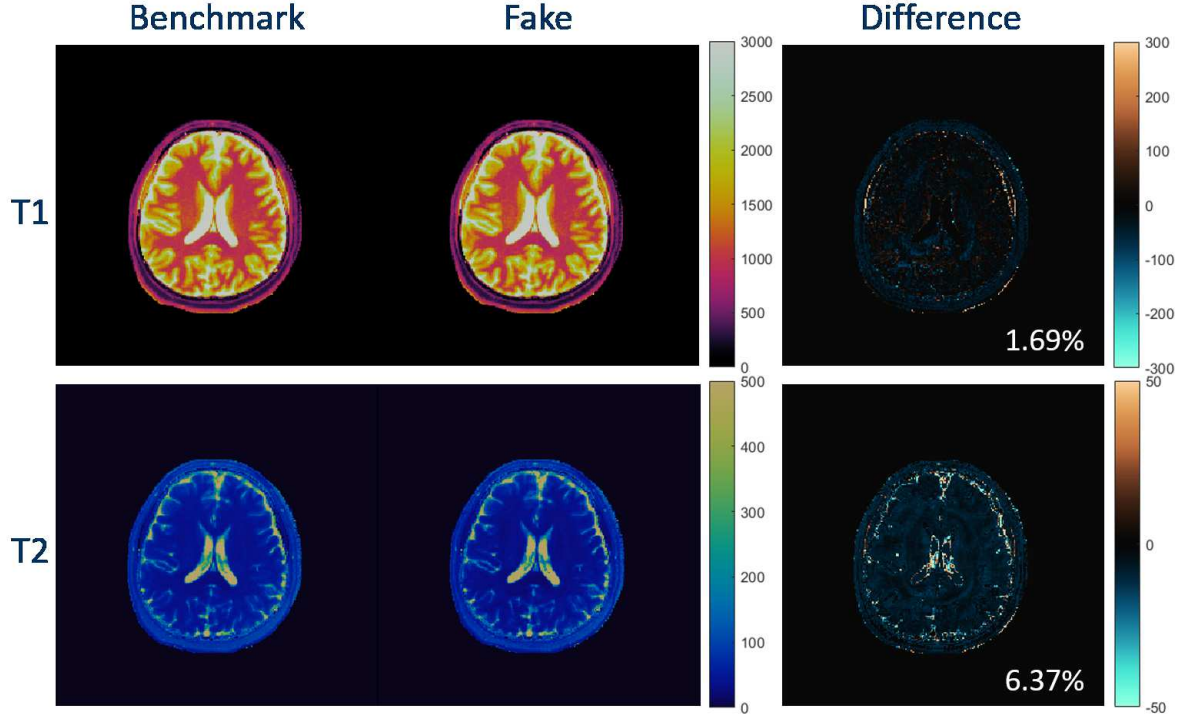


Figure 8: Comparison of maps generated from the fine MRF-FISP dictionary and the GAN-MRF dictionary.

Most importantly for the goals here, we would like to see what advantage the GAN-MRF model can bring in terms of time consumption for MRF dictionary generation. As discussed early, the generation of a slice profile corrected MRF-FISP dictionary requires the simulation of hundreds of spin evolutions which are then added together for each time frame to average out the off resonance effect. This process can take up to hours for a dictionary size of 1000 by 5970 in Matlab depending on the computer hardware. Note that the part of Bloch equation simulations is already coded in the C language. Now by using the GAN-MRF approach, after the GAN-MRF model is trained, it takes only 0.3 second to generate the MRF dictionary with the same size using Python with the Tensorflow framework. This results in tens of thousands times speed up. The time needed for training the GAN-MRF model with the MRF-FISP dictionary of size 1000 by 5970 is 8 hours by using only the Intel Xeon 2.6GHz CPU.

## Discussion

We have described a deep learning approach for MRF dictionary generation based on the state-of-the-art generative adversarial networks. It provides a novel way of mimicking the Bloch equation simulations from MR physics so as to generate the MRF dictionaries more efficiently. We have tested, as an example, the FISP sequence with tissue properties  $T_1$ ,  $T_2$  and sequence parameters flip angle and repetition time as inputs to the model. Our GAN-MRF model reduced the FISP dictionary generation time from hours to sub-second without sacrificing much of the performance. Note that in our experiments, we have only varied the tissue properties  $T_1$  and  $T_2$ . It is also possible to vary the input flip angles and the repetition times. Moreover, we see no obstacle to include more sequence and tissue properties into the GAN-MRF model. Therefore, one should be able to apply this model to problems with more complicated physics for rapid calculation of MRF dictionaries. This may increase the time needed for training, which can be handled with the powerful modern computer capacity, e.g., the use of GPU computing nodes. Once the model is trained, it can be used on a basic to mediocre computer to quickly generate the MRF dictionary. With such a sophisticated deep learning model, we also believe that it is possible to utilize the model for optimization problems arising from the end of MRF sequence parameter design, so that one does not have to tune the sequence parameters heuristically for optimal performance.

Based on the above discussion, one of the immediate applications of the GAN-MRF model is to the more complicated multi-compartment systems, where complicated models such as MRF-X(15) and EPG-X (26) were developed to consider extra properties such as volume fraction, chemical exchange, and magnetization transfer. First, once trained, the GAN-MRF model can help avoid the challenges of generating MRF dictionaries from the complicated models such as the Bloch-McConnell equations in applications, which require specific domain knowledge. Second, a trained GAN-MRF model is much more efficient in generating these MR fingerprints, which can help reduce the turnover time significantly for generating tissue and parameter maps. Moreover, due to the scalability of the GAN-MRF model shown above, the amount of training data needed from these complicated models can be potentially reduced.

Even though our GAN-MRF model has shown great scalability so that one only needs to train the model using a small set of training data in some cases, it is possible in other cases that the training MRF dictionary has a much larger size due to complex physics. In this case, it is possible to combine the GAN-MRF model with other low rank approximation methods such as SVD or randomized



SVD to reduce the memory and time consumption for model training. For instance, one may train the GAN-MRF model with a compressed coarse MRF dictionary using SVD or randomized SVD. The trained model can then be used to synthesize a compressed fine MRF dictionary. The tissue and sequence parameter maps can simply be obtained by applying pattern matching between the compressed in vivo data and the compressed fine dictionary.

The ability of the GAN-MRF model to efficiently mimic the Bloch equations simulated signals has also great implication for clinical applications using MR fingerprinting. For instance, in cardiac MR imaging using MRF, one of the barriers for getting real-time tissue and sequence parameter maps is the inability of standard methods to generate a patient specific MRF dictionary on-the-fly, since different subjects have different heart rates. Therefore, there is no universal MRF dictionary for cardiac scanning. The proposed GAN-MRF model, on the other hand, can synthesize Bloch equations simulated signals in real-time, providing the possibility to generate different MRF dictionaries according to different heart rates on-the-fly by varying the repetition time input of the model.

Last but not least, the scalability of the GAN-MRF model in this paper is mainly tested on the  $T_1$ ,  $T_2$  combinations with the same range except for Fig. 7 and Fig. 8, where the starting range of both  $T_1$  and  $T_2$  for the coarse and fine dictionaries are different. This together with the extrapolation ability of the GAN-MRF model need to be further investigated.

## Conclusions

This work proposed a new approach for MRF dictionary generation based on the recent development in unsupervised learning, namely, the generative adversarial networks (GAN). By comparing to the Bloch equations simulated MRF-FISP fingerprints and the matched  $T_1$ ,  $T_2$  maps, we showed that the proposed GAN-MRF model can generate accurate MRF fingerprints and as a result, accurate  $T_1$ ,  $T_2$  maps with much less computational time. We further demonstrated that this approach is robust enough to generate accurate fine MRF maps using the GAN-MRF model trained from a coarse dictionary. This makes it feasible to generate on-the-fly new MRF fingerprints with tissue property of interest as needed. Moreover, it provides the possibility to significantly reduce the memory and time cost for large scale MRF dictionary generation for more complicated sequence models. It also has great potential for real-time MRF mapping in clinical applications. Furthermore, it opens the door for MRF sequence parameter optimization problems using deep learning techniques.

---

## Acknowledgments

The authors would like to acknowledge funding from Siemens Healthcare, and NIH grants 1R01EB016728-01A1, 5R01EB017219-02.

## References

1. Abadi M, Agarwal A, Barham P, Brevdo E, Chen Z, Citro C, Corrado GS, Davis A, Dean J, Devin M, Ghemawat S, Goodfellow IJ, Harp A, Irving G, Isard M, Jia Y, Józefowicz R, Kaiser L, Kudlur M, Levenberg J, Mané D, Monga R, Moore S, Murray DG, Olah C, Schuster M, Shlens J, Steiner B, Sutskever I, Talwar K, Tucker PA, Vanhoucke V, Vasudevan V, Viégas FB, Vinyals O, Warden P, Wattenberg M, Wicke M, Yu Y, Zheng X. 2016. Tensorflow: Large-scale machine learning on heterogeneous distributed systems. ArXiv:1603.04467. 1603.04467.
2. Cauley SF, Setsompop K, Ma D, Jiang Y, Ye H, Adalsteinsson E, Griswold MA, Wald LL. 2015. Fast group matching for mr fingerprinting reconstruction. *Magnetic Resonance in Medicine* 74:523–528. doi:10.1002/mrm.25439.
3. Chen X, Duan Y, Houthoofd R, Schulman J, Sutskever I, Abbeel P. 2016. Infogan: Interpretable representation learning by information maximizing generative adversarial nets. ArXiv:1606.03657. 1606.03657.
4. Chen Y, Mehta B, Hamilton J, Ma D, Seiberlich N, Griswold M, Gulani V. 2016. Free-breathing 3d abdominal magnetic resonance fingerprinting using navigators. In: *Proceedings of the 24rd Annual Meeting of ISMRM*. Singapore. p. 0716.
5. Chen Y, Pahwa S, Hamilton J, Dastmalchian S, Plecha D, Seiberlich N, Griswold M, Gulani V. 2016. 3d magnetic resonance fingerprinting for quantitative breast imaging. In: *Proceedings of the 24rd Annual Meeting of ISMRM*. Singapore. p. 0399.
6. Cline CC, Chen X, Mailhe B, Wang Q, Nadar M. 2016. Air-mrf: accelerated iterative reconstruction for magnetic resonance fingerprinting. In: *Proceedings of the 24rd Annual Meeting of ISMRM*. Singapore. p. 0434.
7. Cloos MA, Zhao T, Knoll F, Alon L, Lattanzi R, Sodickson DK. 2015. Magnetic resonance

- fingerprint compression. In: Proceedings of the 23rd Annual Meeting of ISMRM. Toronto, Canada.
8. Cohen O, Sarracanie M, Rosen MS, Ackerman JL. 2016. In vivo optimized fast mr fingerprinting in the human brain. In: Proceedings of the 24rd Annual Meeting of ISMRM. Singapore. p. 0430.
  9. Denton EL, Chintala S, szlam a, Fergus R. 2015. Deep generative image models using a laplacian pyramid of adversarial networks. In: C Cortes, ND Lawrence, DD Lee, M Sugiyama, R Garnett, editors. Advances in Neural Information Processing Systems 28. Curran Associates, Inc.. p. 1486–1494.
  10. Doneva M, Amthor T, Koken P, Sommer K, B'ornert P. 2016. Low rank matrix completion-based reconstruction for undersampled magnetic resonance fingerprinting data. In: Proceedings of the 24rd Annual Meeting of ISMRM. Singapore. p. 0432.
  11. Fessler JA, Sutton BP. 2003. Nonuniform fast fourier transforms using min-max interpolation. IEEE Transactions on Signal Processing 51:560–574.
  12. Gómez PA, Buonincontri G, Molina-Romero M, Ulas C, Sperl JI, Menzel MI, Menze BH. 2016. 3d magnetic resonance fingerprinting with a clustered spatiotemporal dictionary. In: Proceedings of the 24rd Annual Meeting of ISMRM. Singapore.
  13. Goodfellow I, Pouget-Abadie J, Mirza M, Xu B, Warde-Farley D, Ozair S, Courville A, Bengio Y. 2014. Generative adversarial nets. In: Z Ghahramani, M Welling, C Cortes, ND Lawrence, KQ Weinberger, editors. Advances in Neural Information Processing Systems 27. Curran Associates, Inc.. p. 2672–2680.
  14. Goodfellow IJ, Pouget-Abadie J, Mirza M, Xu B, Warde-Farley D, Ozair S, Courville A, Bengio Y. 2014. Generative Adversarial Networks. ArXiv:1406.2661. 1406.2661.
  15. Hamilton JI, Griswold MA, Seiberlich N. 2015. Mr fingerprinting with chemical exchange (mrf-x) to quantify subvoxel t1 and extracellular volume fraction. Journal of Cardiovascular Magnetic Resonance 17:1–3. doi:10.1186/1532-429X-17-S1-W35.
  16. Hauser RA, Olanow CW. 1994. Magnetic resonance imaging of neurodegenerative diseases. Journal of Neuroimaging 4:146–158. doi:10.1111/jon199443146.

17. Hernando D, Levin YS, Sirlin CB, Reeder SB. 2014. Quantification of liver iron with mri: State of the art and remaining challenges. *Journal of Magnetic Resonance Imaging* 40:1003–1021. doi:10.1002/jmri.24584.
18. Iles L, Pfluger H, Phrommintikul A, Cherayath J, Aksit P, Gupta SN, Kaye DM, Taylor AJ. 2008. Evaluation of diffuse myocardial fibrosis in heart failure with cardiac magnetic resonance contrast-enhanced t1 mapping. *Journal of the American College of Cardiology* 52:1574–1580. doi:https://doi.org/10.1016/j.jacc.2008.06.049.
19. Isola P, Zhu J, Zhou T, Efros AA. 2016. Image-to-image translation with conditional adversarial networks. *ArXiv:1611.07004*. 1611.07004.
20. Jiang Y, Ma D, Seiberlich N, Gulani V, Griswold MA. 2015. Mr fingerprinting using fast imaging with steady state precession (fisp) with spiral readout. *Magnetic Resonance in Medicine* 74:1621–1631. doi:10.1002/mrm.25559.
21. Kingma DP, Ba J. 2014. Adam: A method for stochastic optimization. *ArXiv:1412.6980*. 1412.6980.
22. Larsson HBW, Frederiksen J, Petersen J, Nordenbo A, Zeeberg I, Henriksen O, Olesen J. 1989. Assessment of demyelination, edema, and gliosis by in vivo determination of t1 and t2 in the brain of patients with acute attack of multiple sclerosis. *Magnetic Resonance in Medicine* 11:337–348. doi:10.1002/mrm.1910110308.
23. Liu F. 2019. Susan: segment unannotated image structure using adversarial network. *Magnetic Resonance in Medicine* 81:3330–3345. doi:10.1002/mrm.27627. <https://onlinelibrary.wiley.com/doi/pdf/10.1002/mrm.27627>.
24. Liu W, Dahnke H, Rahmer J, Jordan EK, Frank JA. 2009. Ultrashort t2\* relaxometry for quantitation of highly concentrated superparamagnetic iron oxide (spio) nanoparticle labeled cells. *Magnetic Resonance in Medicine* 61:761–766. doi:10.1002/mrm.21923.
25. Ma D, Gulani V, Seiberlich N, Liu K, Sunshine JL, Duerk JL, Griswold MA. 2013. Magnetic resonance fingerprinting. *Nature* 495.
26. Malik SJ, Teixeira RPA, Hajnal JV. 2018. Extended phase graph formalism for systems with magnetization transfer and exchange. *Magnetic Resonance in Medicine* 80:767–779. doi:10.1002/mrm.27040. <https://onlinelibrary.wiley.com/doi/pdf/10.1002/mrm.27040>.

27. McGivney DF, Pierre E, Ma D, Jiang Y, Saybasili H, Gulani V, Griswold MA. 2014. Svd compression for magnetic resonance fingerprinting in the time domain. *IEEE Transactions on Medical Imaging* 33:2311–2322. doi:10.1109/TMI.2014.2337321.
28. Odena A, Olah C, Shlens J. 2016. Conditional image synthesis with auxiliary classifier gans. ArXiv:1610.09585.
29. Pahwa S, Lu Z, Dastmalchian S, Jiang Y, Patel M, Meropol N, Griswold M, Gulani V. 2016. Application of magnetic resonance fingerprinting (MRF) for assessment of rectal cancer: a feasibility study. In: *Proceedings of the 24rd Annual Meeting of ISMRM*. Singapore. p. 2966.
30. Payne AR, Berry C, Kellman P, Anderson R, Hsu LY, Chen MY, McPhaden AR, Watkins S, Schenke W, Wright V, Lederman RJ, Aletras AH, Arai AE. 2011. Bright-blood t2-weighted mri has high diagnostic accuracy for myocardial hemorrhage in myocardial infarctionclinical perspective. *Circulation: Cardiovascular Imaging* 4:738–745. doi:10.1161/CIRCIMAGING.111.965095. <http://circimaging.ahajournals.org/content/4/6/738.full.pdf>.
31. Radford A, Metz L, Chintala S. 2015. Unsupervised representation learning with deep convolutional generative adversarial networks. ArXiv:1511.06434. 1511.06434.
32. Reed SE, Akata Z, Yan X, Logeswaran L, Schiele B, Lee H. 2016. Generative adversarial text to image synthesis. ArXiv:1605.05396. 1605.05396.
33. Reeder SB, Cruite I, Hamilton G, Sirlin CB. 2011. Quantitative assessment of liver fat with magnetic resonance imaging and spectroscopy. *Journal of Magnetic Resonance Imaging* 34:729–749. doi:10.1002/jmri.22775.
34. Salimans T, Goodfellow IJ, Zaremba W, Cheung V, Radford A, Chen X. 2016. Improved techniques for training gans. ArXiv:1606.03498. 1606.03498.
35. Souza RB, Feeley BT, Zarins ZA, Link TM, Li X, Majumdar S. 2013. T1rho mri relaxation in knee oa subjects with varying sizes of cartilage lesions. *The Knee* 20:113–119.
36. Usman AA, Taimen K, Wasielewski M, McDonald J, Shah S, Giri S, Cotts W, McGee E, Gordon R, Collins JD, Markl M, Carr JC. 2012. Cardiac magnetic resonance t2 mapping in the monitoring and follow-up of acute cardiac transplant rejectionclinical perspective. *Circulation: Cardiovascular Imaging* 5:782–790. doi:10.1161/CIRCIMAGING.111.971101. <http://circimaging.ahajournals.org/content/5/6/782.full.pdf>.

37. van Heeswijk RB, Feliciano H, Bongard C, Bonanno G, Coppo S, Lauriers N, Locca D, Schwitter J, Stuber M. 2012. Free-breathing 3 t magnetic resonance t2-mapping of the heart. *JACC: Cardiovascular Imaging* 5:1231–1239. doi:<https://doi.org/10.1016/j.jcmg.2012.06.010>.
38. Yang M, Ma D, Jiang Y, Hamilton J, Seiberlich N, Griswold MA, McGivney D. 2018. Low rank approximation methods for mr fingerprinting with large scale dictionaries. *Magnetic Resonance in Medicine* 79:2392–2400. doi:10.1002/mrm.26867.
39. Zhang X, Li R, Hu X. 2016. Mr fingerprinting reconstruction with kalman filter. In: *Proceedings of the 24rd Annual Meeting of ISMRM*. Singapore. p. 0436.
40. Zhao B, Haldar JP, Setsompop K, Wald LL. 2016. Optimal experiment design for magnetic resonance fingerprinting. In: *2016 38th Annual International Conference of the IEEE Engineering in Medicine and Biology Society (EMBC)*. p. 453–456. doi:10.1109/EMBC.2016.7590737.
41. Zhao B, Setsompop K, Gagoski B, Ye H, Adalsteinsson E, Grant PE, Wald LL. 2016. A model-based approach to accelerated magnetic resonance fingerprinting time series reconstruction. In: *Proceedings of the 24rd Annual Meeting of ISMRM*. Singapore. p. 0871.
42. Zhao JJ, Mathieu M, LeCun Y. 2016. Energy-based generative adversarial network. *ArXiv:1609.03126*. 1609.03126.